(Di)Triazolylidene Manganese Complexes in Catalytic Oxidation of Alcohols to Ketones and Aldehydes

Mara F. Pinto,[a] Marta Olivares,[b] Angela Vivancos,[b] Gregorio Guisado-Barrios,[c] Martin Albrecht [b]* and Beatriz Royo [a]*

a) Instituto de Tecnologia Química e Biológica António Xavier, ITQB NOVA, Universidade Nova de Lisboa, Av. da República, 2780-157 Oeiras, Portugal.

b) Department of Chemistry & Biochemistry, University of Bern, Freiestrasse 3, 3012 Bern, Switzerland

c) Institute of Advanced Materials (INAM), Universitat Jaume I, 12071 Castellon, Spain

Electronic Supplementary Information:

1. Synthesis and characterization of complexes 2 and 3

General Considerations

The synthesis of complexes **2** and **3** was performed under a nitrogen atmosphere using standard Schlenk techniques, and solvents were purified from appropriate drying agents and distilled under nitrogen. Deuterated solvents were degassed and stored over molecular sieves. The ditriazolium triflate salts **1a**,[S1] **1b**,[S2] ditriazolium bromide salts of **1a** and **1b**,[S3] and the manganese complex **4**[S4] were synthesized according to the methods described in the literature. All other reagents were purchased from commercial suppliers and used without further purification. $[MnBr(CO)_5]$ was purchased from Strem chemicals and used as received. ^1H and ^{13}C NMR spectra were recorded with a Bruker Avance III 400 MHz. Electrospray mass spectra (ESI-MS) were recorded with a Micromass Quatro LC instrument; nitrogen was employed as a drying and nebulizing gas. Elemental analyses were performed in the laboratories at ITQB.

Preparation of (di-trz)MnBr(CO)$_3$ (2)

The ditriazolium triflate salt **1a** (0.60 g, 0.86 mmol) was dissolved in a minimum amount of dry acetone and treated with tetra(*n*-butyl) ammonium bromide (0.58 g, 1.8 mmol). After stirring for few minutes, the ditriazolium bromide salt precipitated. It was isolated by filtration, washed with acetone, dried under vacuum and weighed (0.40 g, 0.71 mmol, 83% yield). Solid MnBr(CO)$_5$ (0.25 g, 0.90 mmol) was suspended in THF (15 mL) and potassium *tert*-butoxide (0.18 g, 1.6 mmol) was added first, followed by addition of the corresponding ditriazolium bromide (0.40 g, 0.71 mmol) at 60 °C. The resulting suspension was heated at 60 °C for 16 h under stirring. All volatiles were removed under vacuum and the resulting residue was washed with toluene (4 x 15 mL) and dissolved in dichloromethane (80 mL). The dichloromethane solution was washed with water (80 mL), and the organic extract was dried with Na_2SO_4. The solution was filtered and concentrated to dryness under vacuum to yield a yellow-orange powder. Yield: 0.20 g, 45%. ^{1}H NMR (DMSO-d$_6$, 25 °C): δ 7.11, 7.09 (2 × s, 2H, Ar-C$_6$*H*$_2$), 4.71 (s, 6H, NC*H*$_3$), 2.33 (s, 6H, C*H*$_3$), 2.16 (s, 6H, C*H*$_3$), 2.02 (s, 6H, C*H*$_3$). ^{13}C NMR (DMSO-d$_6$, 25 °C): δ 220.40 (*C*O), 196.28 (C_{trz-Mn}), 141.22 (C_{Ph}), 139.71 (C_{trz}-C_{trz}), 135.82 (C_{Ph}), 134.96 (C_{Ph}), 134.40 (C_{Ph}), 128.96 (C_{Ph}), 128.54 (C_{Ph}), 38.7 (N*C*H$_3$) 20.76 (*C*H$_3$), 18.01 (*C*H$_3$), 16.68 (*C*H$_3$), one CO not resolved. IR (KBr): υ(CO) 2004, 1918, 1884 cm^{-1}. Anal. Calcd. for $C_{27}H_{28}MnN_6O_3Br.CH_2Cl_2$: C, 47.73; H, 4.29; N, 11.93. Found: C, 47.50; H, 4.84; N, 12.21.

Preparation of (μ-di-trz)Mn$_2$(CO)$_8$ (3)

The ditriazolium triflate salt **1b** (0.43 g, 0.83 mmol) was dissolved in a minimum amount of dry acetone and treated with tetra(*n*-butyl) ammonium bromide (0.56 g, 1.7 mmol). After stirring for few minutes, the ditriazolium bromide salt precipitated. It was isolated by filtration, washed with acetone, dried under vacuum and weighed (0.24 g, 0.63 mmol, 76% yield). Solid MnBr(CO)$_5$ (0.22 g, 0.80 mmol) was suspended in THF (15 mL) and potassium *tert*-butoxide (0.16 g, 1.4 mmol) was added first, followed by addition of the corresponding ditriazolium bromide (0.24 g, 0.63 mmol) at 60 °C. The resulting suspension was heated at 60 °C for 16 h under stirring. All volatiles were removed under vacuum and the resulting residue was washed with toluene (4 x 15 mL) and dissolved in dichloromethane (80 mL). The dichloromethane solution was washed with water (80 mL), and the organic extract was dried with Na_2SO_4. The solution was filtered and concentrated to dryness under vacuum to yield a yellow-orange powder. Yield: 0.18 g, 52%. ^{1}H NMR (DMSO-d$_6$, 25 °C): δ 4.77 (m, 4H, NC*H*$_2$CH$_3$), 4.15 (s, 6H, NC*H*$_3$), 1.63 (t, 6H, NCH$_2$C*H*$_3$). ^{13}C NMR (DMSO-d$_6$, 25 °C): δ 231.26 (*C*O), 229.32 (*C*O), 225.36 (*C*O), 223.27 (*C*O), 181.15 (C_{trz-Mn}), 138.03 (C_{trz}-C_{trz}), 48.88 (N *C*H$_2$CH$_3$), 38.56 (N*C*H$_3$), 15.38 (NCH$_2$*C*H$_3$). IR (KBr): υ(CO) 2035, 1971, 1912, 1881 cm^{-1}. Anal. Calcd. for $C_{18}H_{16}Mn_2N_6O_8$: C, 38.99; H, 2.91; N, 15.16. Found: C, 38.40; H, 3.27; N, 15.30.

NMR and IR spectra of complexes **2** and **3**:

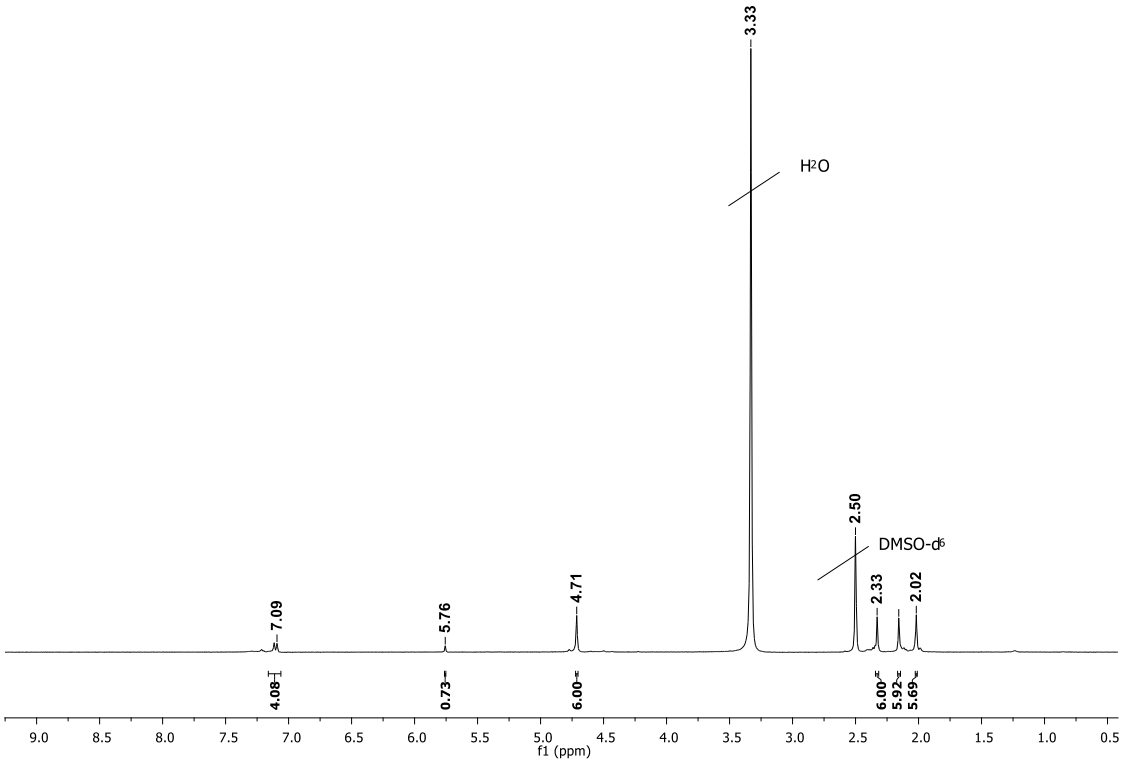

Figure S1. ^{1}H NMR spectrum of **2** at 25 °C in DMSO-d_6.

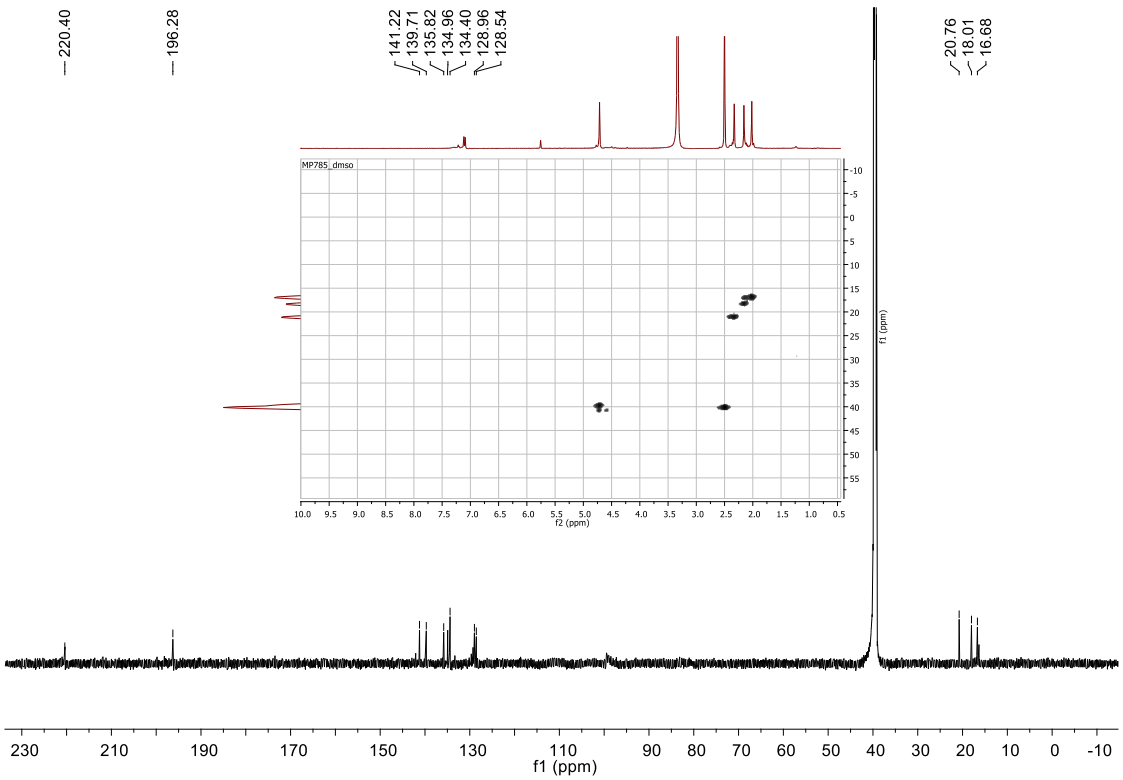

Figure S2. ^{13}C{^{1}H} NMR spectrum of **2** at 25 °C in DMSO-d_6; insight shows selected range of HSQC spectrum indicating the coinciding ^{13}C NMR frequency of the N–CH_3 group and the DMSO.

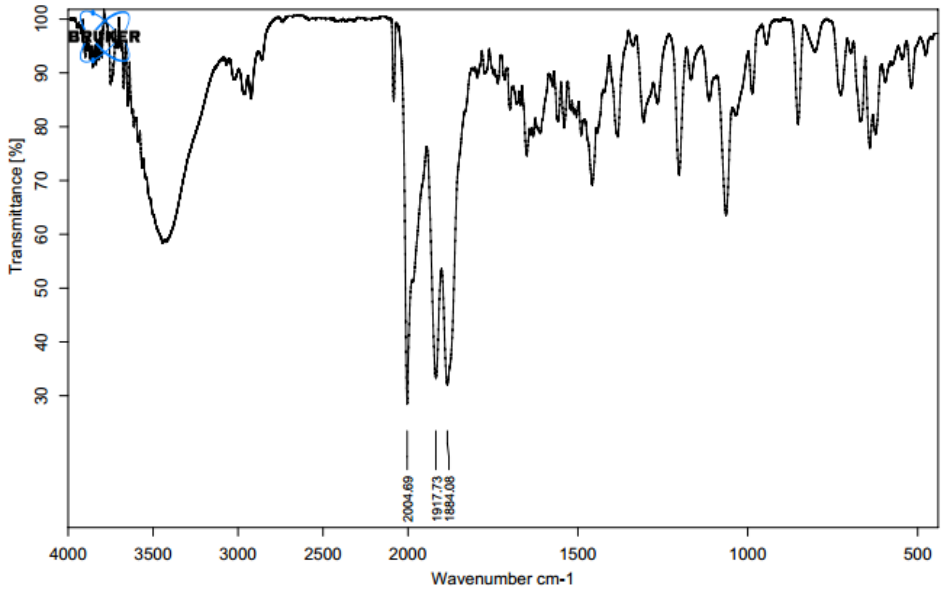

Figure S3. IR spectrum of **2** in KBr.

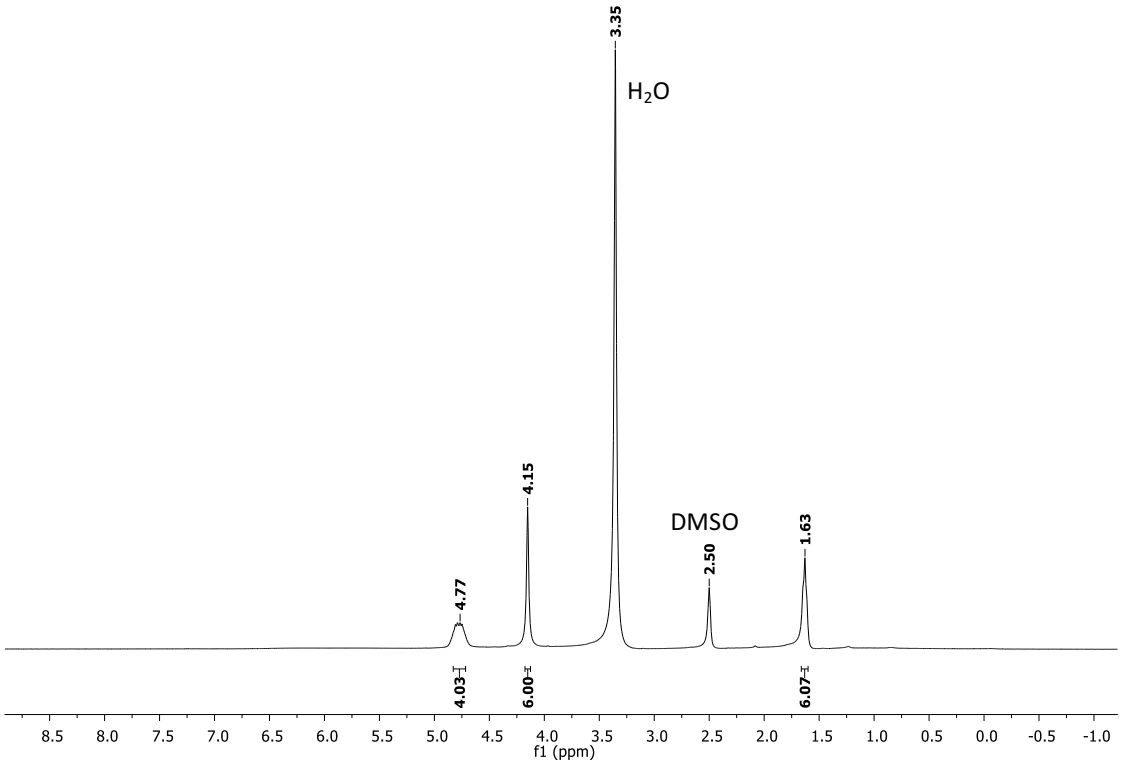

Figure S4. ^{1}H NMR spectrum of **3** at 25 °C in DMSO-d_6.

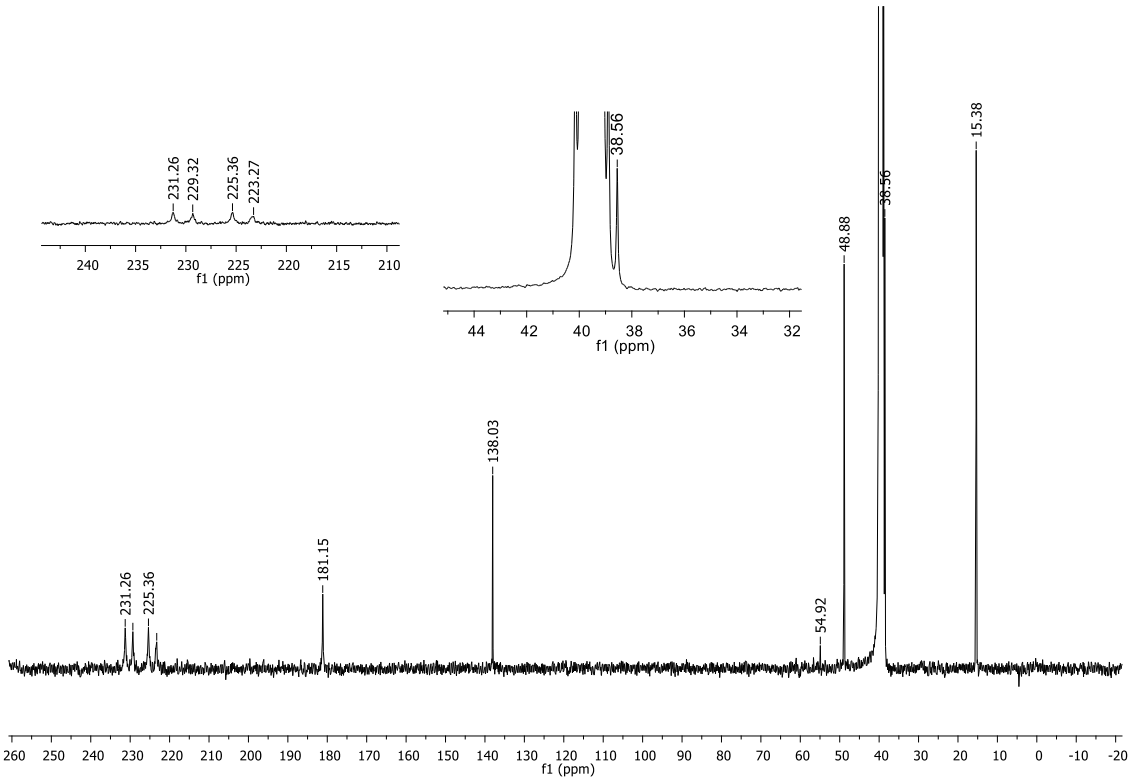

Figure S5. $^{13}C\{^{1}H\}$ NMR spectrum of **3** at 25 °C in DMSO-d_6.

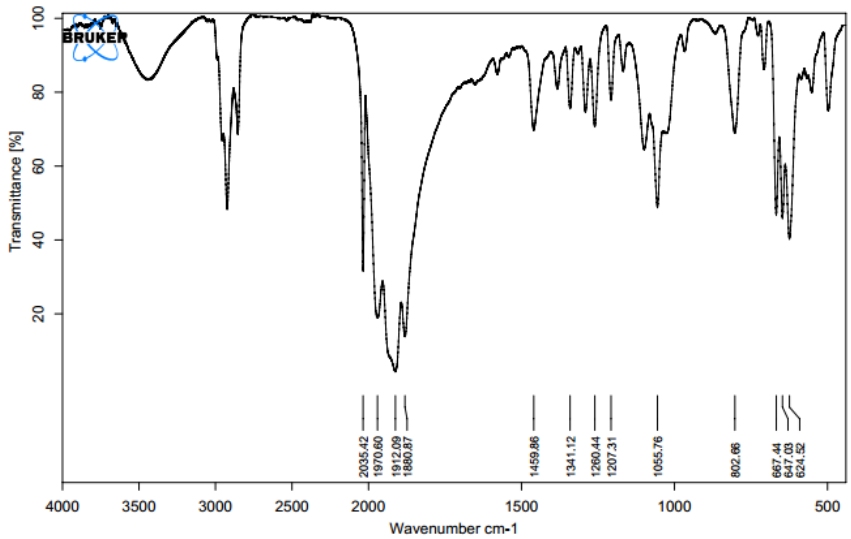

Figure S6. IR spectrum of **3** in KBr.

2. Catalytic procedures

Typical procedure for catalytic alcohol oxidation.
A flask was charged in open air with catalyst (1 mol%) and substrate (0.5 mmol). Then, TBHP (5.0–6.0 M in decane, 0.75 mmol) and acetonitrile (0.4 mL) were added. The progress of the reaction was monitored by taking aliquots of the reaction mixtures and subjecting them to ^{1}H NMR analysis in $CDCl_3$. The yield was determined by ^{1}H NMR spectroscopy using mesitylene as an internal standard. In some cases, the yield was determined by GC. The corresponding products were extracted in dichloromethane, filtered and the residue dried under vacuum. The products were identified by comparison of their NMR spectral data to the literature.

Optimization of the catalytic conditions are compiled in Figures S7–S12.

Variation of temperature

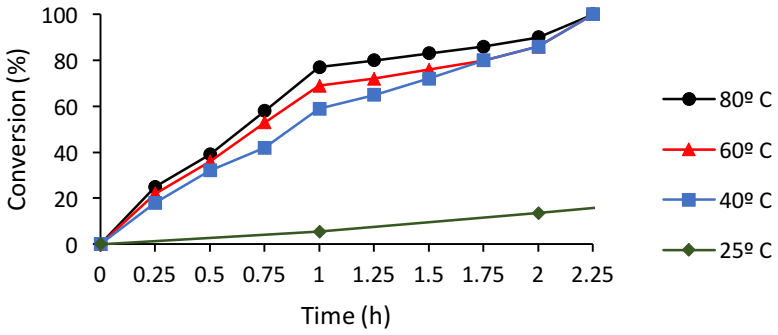

Figure S7. Kinetic profiles of complex **3** in the oxidation of 1-phenylethanol with TBHP in acetonitrile at different temperatures. Reaction conditions: 1-Phenylethanol (0.5 mmol), **3** (1 mol%), TBHP (0.75 mmol), acetonitrile (0.4 mL); conversions determined by ^{1}H NMR spectroscopy.

Variation of solvent

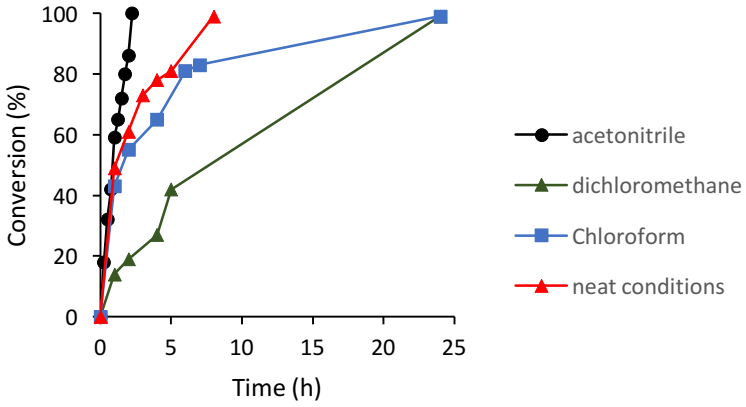

Figure S8. Kinetic profiles of complex **3** in the oxidation of 1-phenylethanol with TBHP at 40 °C in different solvents. Reaction conditions: 1-Phenylethanol (0.5 mmol), **3** (1 mol%), TBHP (0.75 mmol), solvent (0.4 mL) at 40 °C; conversions determined by ^{1}H NMR spectroscopy.

Variation of catalyst loading

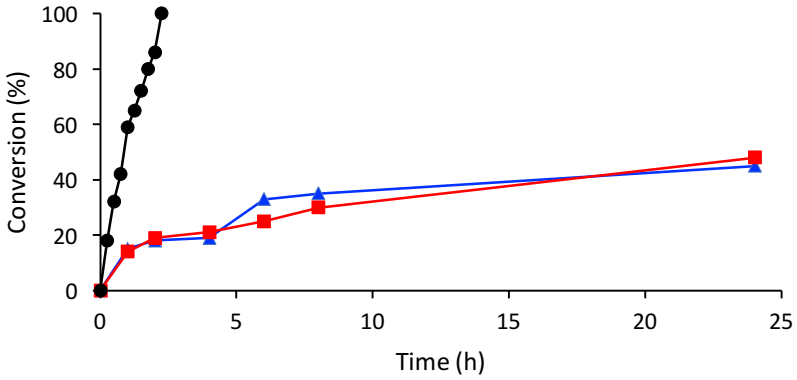

Figure S9. Kinetic profiles of complex **3** in the oxidation of 1-phenylethanol with TBHP at 40 °C in acetonitrile using different catalyst loadings. Black trace: 1-phenylethanol (1 mmol), TBHP (1.5 mmol), **3** (0.01 mmol; 1 mol%); Blue trace: 1-phenylethanol (1 mmol), TBHP (1.5 mmol), **3** (0.005 mmol; 0.5 mol%); Red trace: 1-phenylethanol (2 mmol), TBHP (3.0 mmol), **3** (0.01 mmol; 0.5 mol%); conversions determined by ^{1}H NMR spectroscopy.

Variation of oxidant ratio

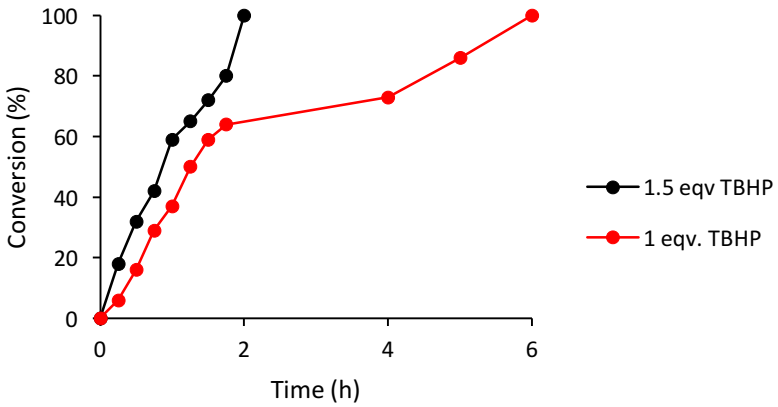

Figure S10. Kinetic profiles of complex **3** in the oxidation of 1-phenylethanol at 40 °C in acetonitrile with TBHP. Black trace: 1-phenylethanol (1 mmol), TBHP (1.5 mmol), **3** (1 mol%); Red trace: 1-phenylethanol (1 mmol), TBHP (1 mmol), **3** (1 mol%); conversions determined by ^{1}H NMR spectroscopy.

Recycling of the catalyst

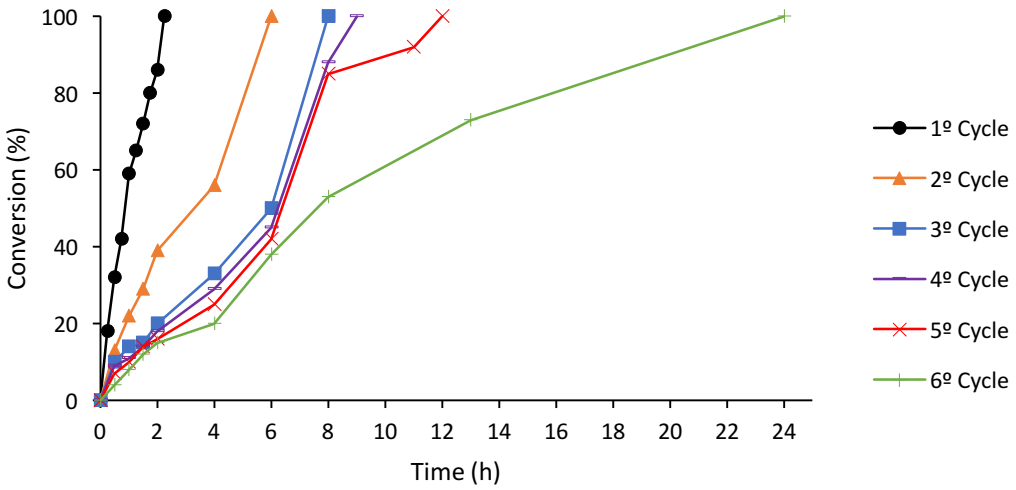

Figure S11. Reuse of catalyst **3**. Time-conversion profile for the oxidation of 1-phenylethanol catalysed by **3** when adding new charges of substrate (1 mmol) and TBHP (1.5 mmol) after each cycle. Reaction performed with **3** (1 mol%), acetonitrile (0.4 mL) at 40 °C; conversions determined by ^{1}H NMR spectroscopy.

Mercury poisoning experiments

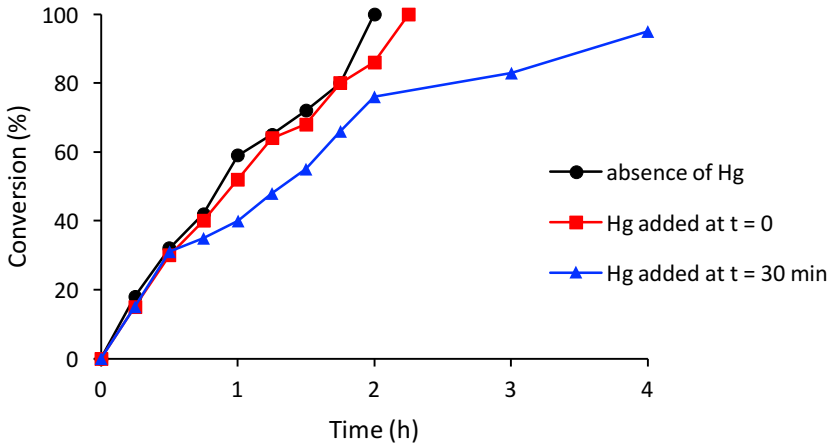

Figure S12. Time-conversion profile (^{1}H NMR monitoring) for the oxidation of 1-phenylethanol catalyzed by **3** with TBHP in the presence of Hg (>1000 eqv.); all conversions determined by ^{1}H NMR spectroscopy

Black trace: typical procedure under standard conditions using 1-phenylethanol (0.5 mmol), TBHP (0.75 mmol), complex **3** (1 mol%).

Red trace: typical procedure with Hg added at the onset of the reaction. Elemental mercury (>1 g, >5 mmol) was added to complex **3** (2.77 mg, 0.005 mmol, 1 mol%) and 1-phenylethanol (0.06 mL, 0.5 mmol). Then, TBHP (0.15 mL, 5.0–6.0 M in decane, 0.75 mmol) and acetonitrile (0.4 mL) were added and the reaction mixture was heated to 40 °C.

Blue trace: typical procedure with Hg added at 30% conversion. 1-phenylethanol (0.06 mL, 0.5 mmol), TBHP (0.15 mL, 5.0–6.0 M in decane, 0.75 mmol), and complex **3** (2.77 mg, 0.005 mmol) were dissolved in acetonitrile (0.4 mL) and the reaction mixture was heated to 40 °C. After 30 min, Hg (>1 g, >5 mmol) was added and stirring of the reaction at 40 °C was continued.

Table S1. Reported Mn-catalysed oxidation of benzyl alcohol to benzaldehyde

entry	cat	TON	TOF /h^{-1}	yield	selectiv	loading	conditions	ref
1	$Mn^{II}(N_4)X_2$	97	170 [a]	47%	79%	0.5 mol%	H_2O_2 (4 equiv), AcOH (10 equiv)	S5
2	$[Mn^{V}(N)(CN)_4]^{2-}$	66	133 [a]	<10%	n.d. [b]	0.1 mol%	Co^{III}/Ru^{II} photocatalytic, buffer	S6
3	$Mn^{II}(N_4)X_2$	86	43 [a]	86%	n.d. [b]	1 mol%	H_2O_2 (6 equiv), acid (0.5 equiv) [c]	S7
4	$Mn^{II}(NO_3)_2$	25	8 [a]	100%	>98%	4 mol%	TEMPO (5 mol%), pyrCOOH [d]	S8
5	$Mn^{II}(NO_3)_2$	450	84	100%	n.d. [b]	2 mol%	TEMPO (2mol%), pyrCOOH, $NaNO_3$ [d]	S9
6	$Mn^{II}(N_4)Cl_2$	80	14 [a]	37%	86%	0.5 mol%	H_2O_2 (4 equiv), $HNO_{3\,aq}$,	S10
7	MnO_2	0.1	---	77%	n.d. [b]	10 equiv	no other oxidant	S11
8	$Mn^{III}(N_2O_2)Cl$	1000 [e]	960 min^{-1}	50%	n.d. [b]	0.05 mol%	$(NBu_4)HSO_5$ (1.7 equiv), MeCN	S12
9	$Mn^{III}(N_2O_2)Cl$	100	2000 [a,e]	95%	>95%	1 mol%	$(NBu_4)HSO_5$ (1.7 equiv), MeCN	S12
10	$Mn^{II}(N_4)X_2$	170	74	85%	86%	0.5 mol%	H_2O_2 (1 equiv), MeCN	S13
11	$Mn(bpy)_2X_2$	152	n.a.	90%	52%	0.8 mol%	TBHP (1.6 mol%)	S14
12	**3**	84	25	84%	96%	1 mol%	TBHP (1.5 equiv), MeCN	*this work*

n.d. = not discussed
[a] estimated TOF based on the single time/conversion point provided in the article
[b] n.d. = not discussed, selectivity unclear
[c] acid = adamantyl-COOH, only cinnamylalcohol (conjugated alcohol) as substrate
[d] AcOH as solvent, aerobic conditions, only substituted BnOH as substrate
[e] The Haddad system (entries 8,9) is peculiar with phenomenally high rates, but also conversions that seem to take place only in the first seconds of the reaction, but this unusual behavior has not been addressed

Earlier report on 100% selectivity and yield with a Mn^{II}(terpy)Cl2(H2O) complex[S11] was found to be heterogeneous in nature[S12] and is therefore not listed in Table S1. Entries 8 and 9 report very high activity, though the absence of kinetic data do not allow for differentiating between a homogeneous catalyst and a heterogeneization (with an apparent turnover of 1000 within the first min, and then no turnovers for the subsequent 2 h). The notion of a heterogeneous catalyst is supported by the previously noted tendency of Mn complexes with N-donor ligands to heterogeneize during activation.[S12]

Table S2. Reported Mn-catalysed oxidation of 1-phenylethanol to acetophenone

entry	cat	TON	TOF	yield	loading	conditions	ref
1	$Mn^{II}(N_4)X_2$	200	400 [a]	84%	0.5 mol%	H_2O_2 (4 equiv), AcOH (10 equiv)	S5
2	$[Mn^{V}(N)(CN)_4]^{2-}$	44	88 [a]	<5%	0.1 mol%	Co^{III}/Ru^{II} photocatalytic, phosphate buffer	S6
3	$Mn^{II}(N_4)X_2$	95	47 [a]	95%	2.5 mol%	H_2O_2 (6 equiv), adamantylCOOH (0.5 equiv)	S7
4	$Mn^{II}(NO_3)_2$	25	9 [a]	100%	4 mol%	TEMPO (5 mol%), pyrCOOH (6 mol%) [b]	S8
5	$Mn^{II}(NO_3)_2$	49	18 [a]	100%	2mol%	TEMPO (2 mol%), pyrCOOH (3 mol%), $NaNO_3$ [b]	S9
6	$Mn^{II}(N_4)Cl_2$	84	14 [a]	39%	0.5 mol%	H_2O_2 (4 equiv), $HNO_{3\,aq}$	S10
7	$Mn^{III}(N_2O_2)Cl$	100	6000 [a]	100%	1 mol%	$(NBu_4)HSO_5$ (1.7 equiv), MeCN	S12
8	$Mn^{II}(N_4)X_2$	98	25 [a]	49%	0.5 mol%	H_2O_2 (1 equiv), MeCN	S13
9	$Mn(N_4)X_2$	4,700	2000 [a,c]	99%	0.05 mol%	H_2O_2 (1.5 equiv), HOAc (1 equiv), MeCN	S17
10	$Mn(N_4)X_2$	450	320 [a]	93%	0.3 mol%	H_2O_2 (1.2 equiv), H_2SO_4 (0.3 equiv), MeCN	S18
11	$Mn(OAc)_2$	56	7 [a]	100%	1.8 mol%	TBHP (2.5 equiv), TFA (0.1 equiv)	S19
12	**3**	600	72	100%	1 mol%	TBHP (1.1 equiv), MeCN	*this work*

[a] estimated TOF based on single time/conversion point provided in the article
[b] in air and with AcOH as solvent
[c] unlikely to be a well-defined homogeneous catalyst, see comments to Table S1.

3. NMR spectra of the products isolated from the catalytic oxidation of alcohols using 3 as catalyst

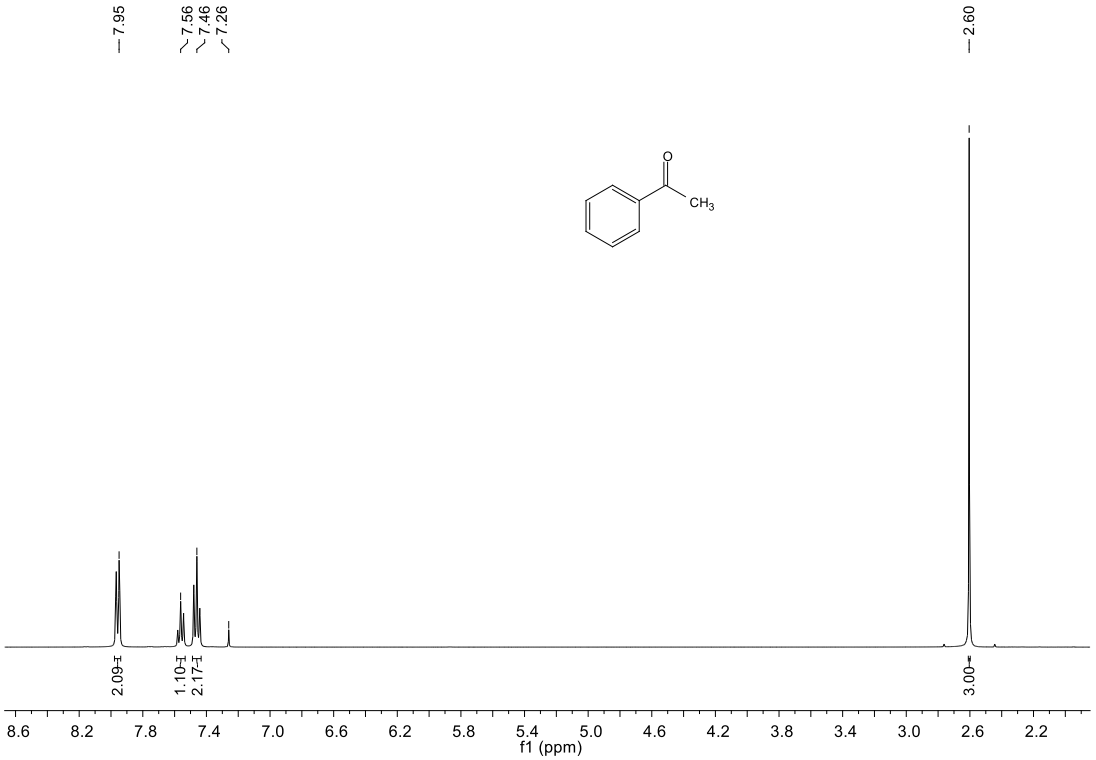

Figure S13. ^{1}H NMR spectrum of acetophenone ($CDCl_3$, 400 MHz).

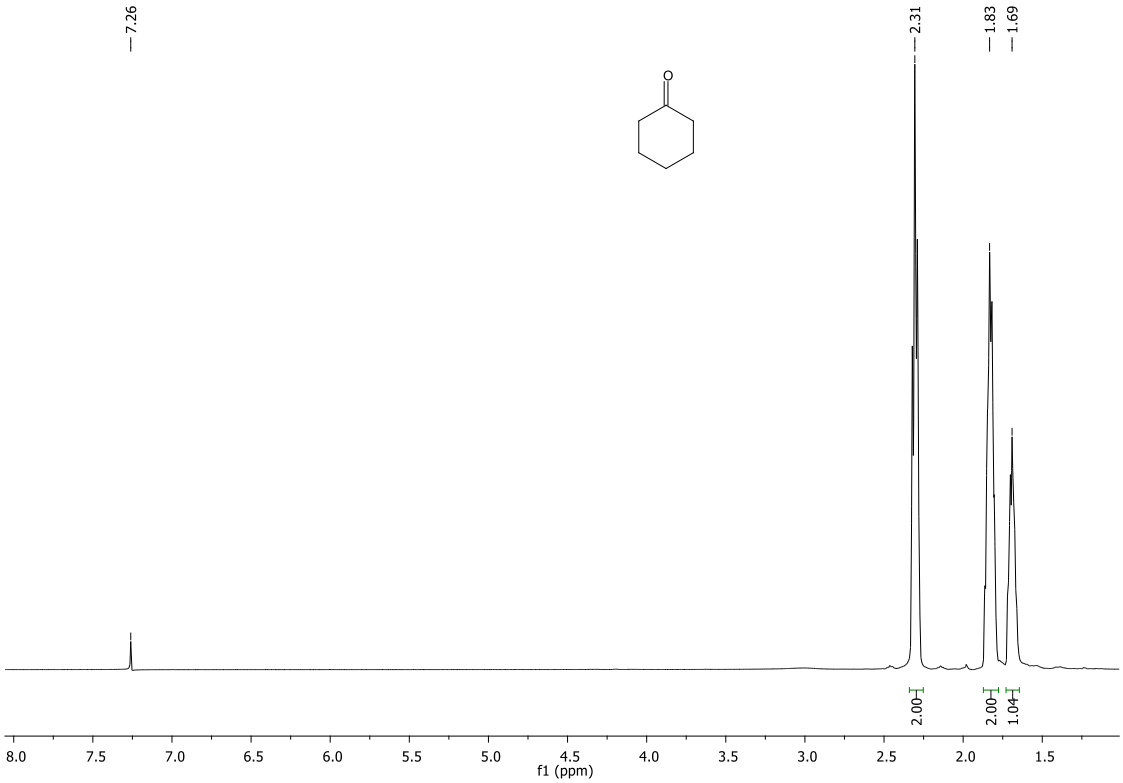

Figure S14. ^{1}H NMR spectrum of cyclohexanone ($CDCl_3$, 400 MHz).

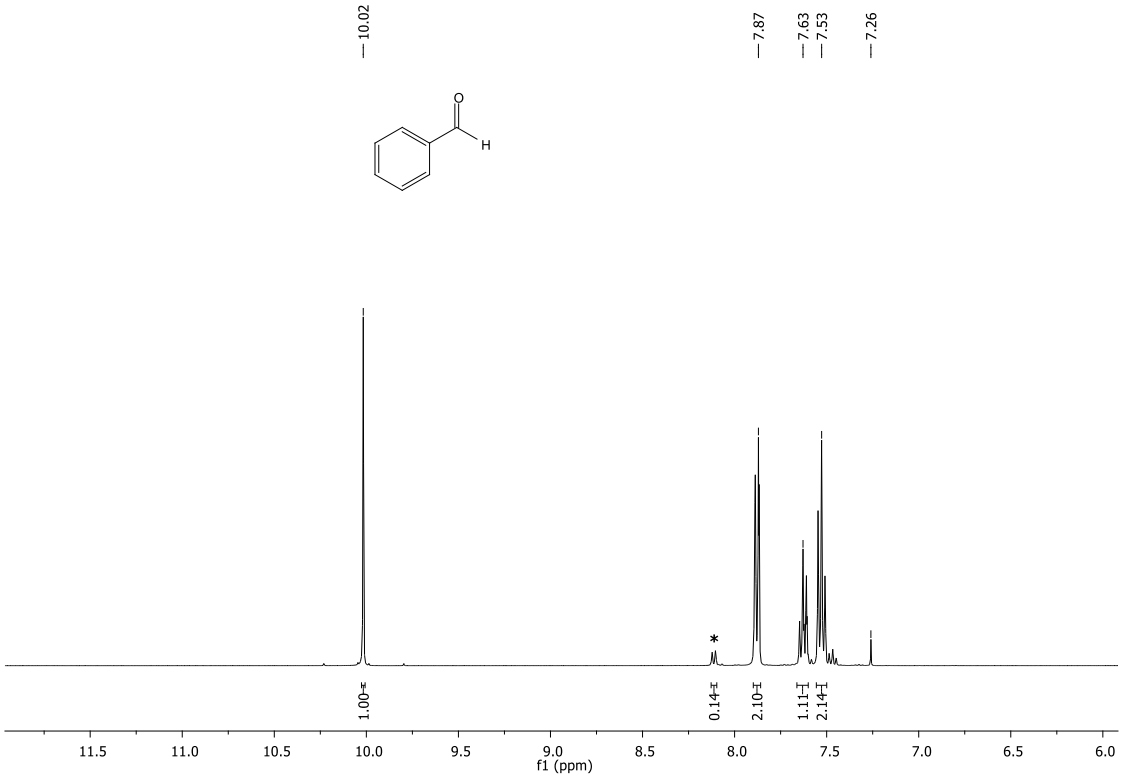

Figure S15. ^{1}H NMR spectrum of benzaldehyde ($CDCl_3$, 400 MHz). *Benzoic acid

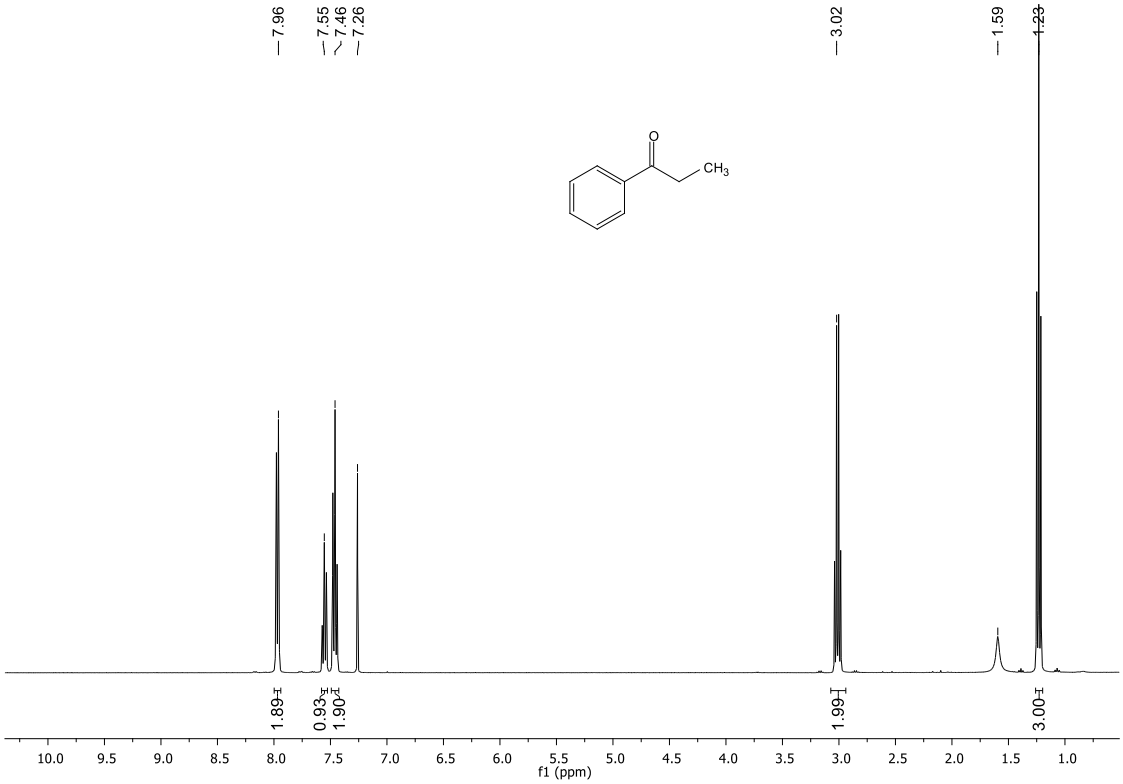

Figure S16. ^{1}H NMR spectrum of propiophenone ($CDCl_3$, 400 MHz).

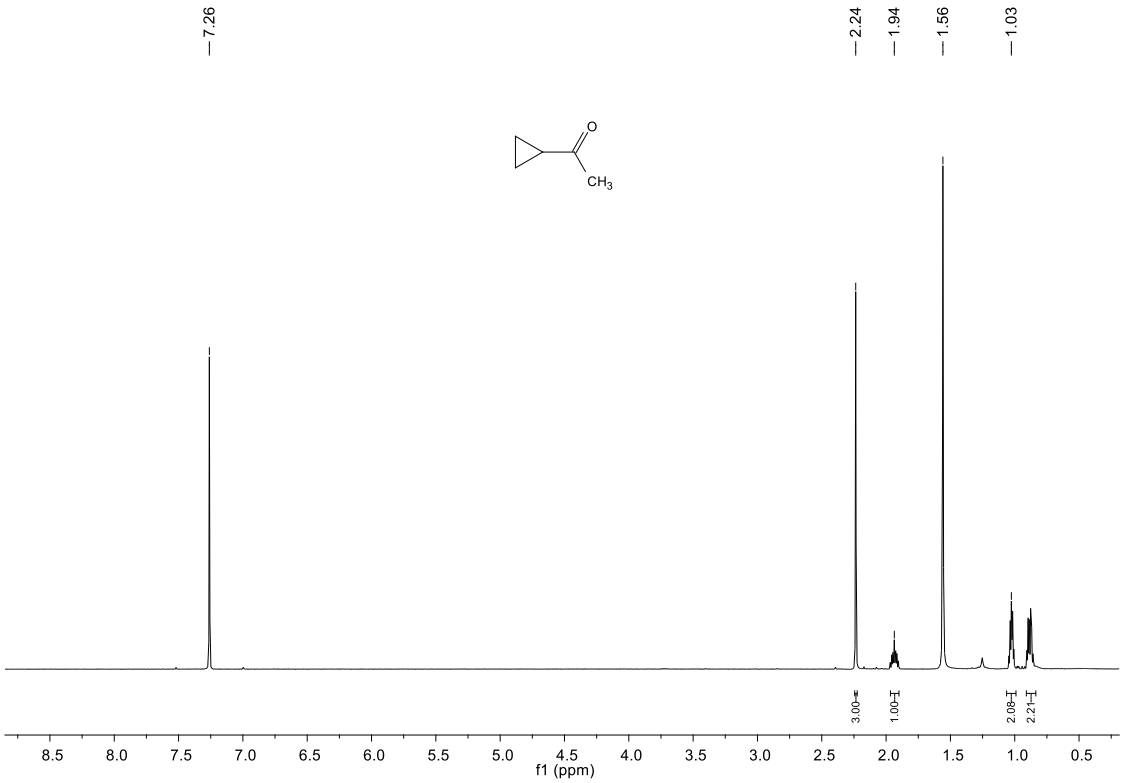

Figure S17. ^{1}H NMR spectrum of cyclopropyl methyl ketone ($CDCl_3$, 400 MHz).

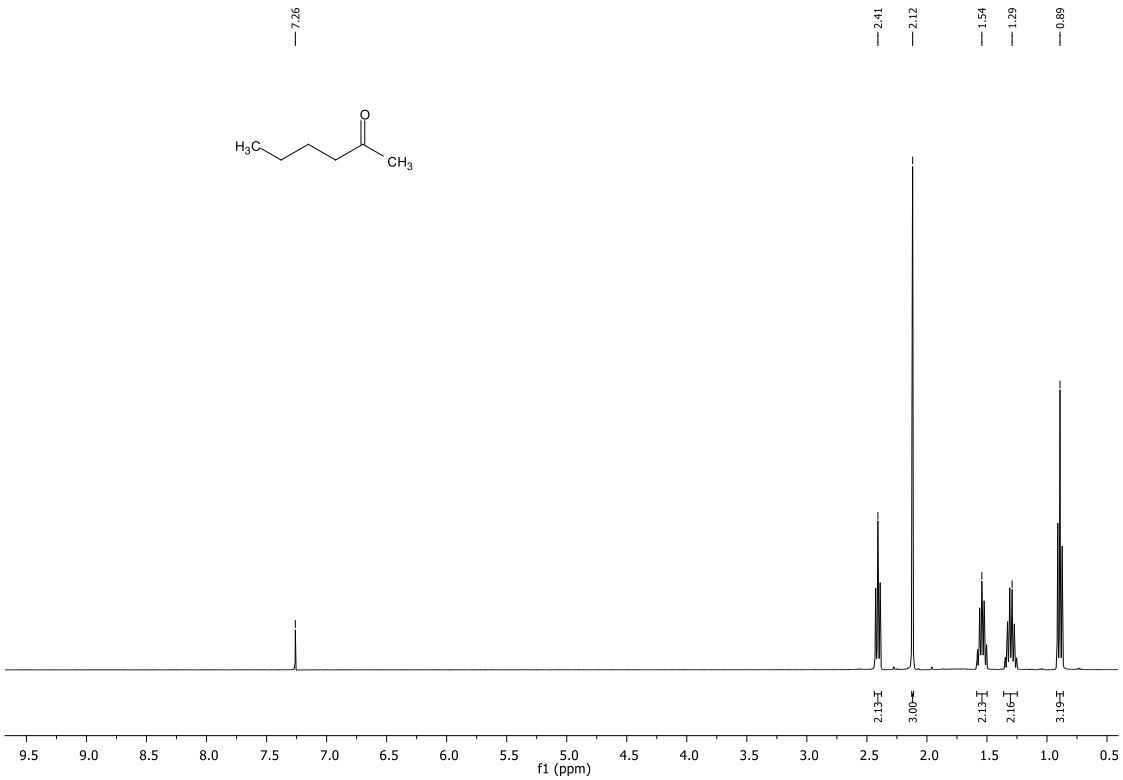

Figure S18. ^{1}H NMR spectrum of 2-hexanone ($CDCl_3$, 400 MHz).

4. Electrochemical analysis of complexes 2–5

Cyclic voltammetry (CV) and differential pulse voltammetry (DPV) measurements were carried out using a Metrohm Autolab Model PGSTAT101 potentiostat employing a three electrode cell under an argon atmosphere. A platinum electrode with 7.0 mm^2 surface area was used as the working electrode. The reference electrode was Ag/AgCl; the counter electrode was Pt wire. $[NBu_4]PF_6$ (0.1 M) in dry MeCN was used as supporting electrolyte. All voltammograms are referenced to ferrocene/ferrocenium (Fc/Fc^+) using either Fc or $[Ru(bpy)_3]^{2+}$ as internal standard (2 mg standard added after each measurement). The oxidation potential of **[**$Ru(bpy)_3](PF_6)_2$ *vs* Fc/Fc^+ was determined in MeCN to use this complex as an internal standard when Fc was not suitable, providing $E_{1/2}$ = +0.89 V *vs* Fc^+/Fc (Fig. S19). Data pertaining to complex **2** are shown in Fig. S20–S24 and Table S3; to complex **3** in Fig. S25–S27 and Table S4; to complex **4** in Fig. S28–S29 and Table S5, and to complex **5** in Fig. S30.

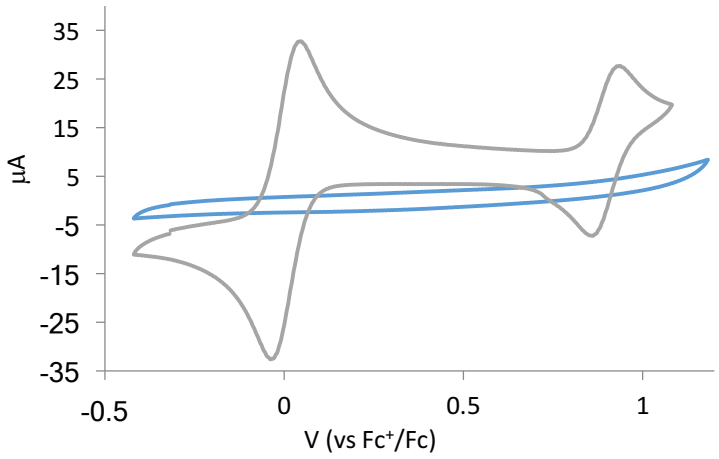

Figure S19. Overlaid CV plots of 0.5 mM solutions of $[Ru(bpy)_3](PF_6)_2$ and Ferrocene (grey), and blank solution (blue) in 0.1 M $[NBu_4]PF_6$ in MeCN, scan rate 500 mV s^{-1}.

*Complex **2***

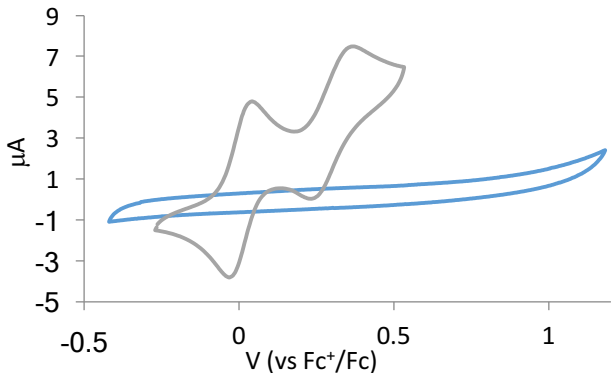

Figure S20. Overlaid CV plots of 0.5 mM solutions of complex **2** and ferrocene as internal standard (grey), and blank solution (blue) in 0.1 M $[NBu_4]PF_6$ in MeCN, scan rate 100 mV s^{-1}.

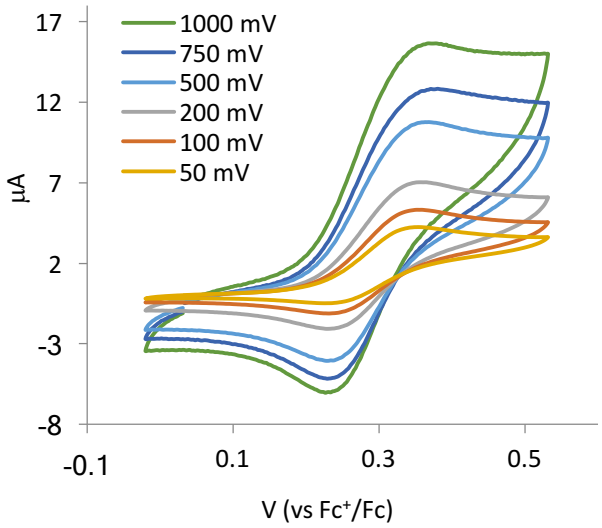

Figure S21. Overlaid CV plots of 0.5 mM solutions of complex **2** at 50 to 1000 mV s^{-1} scan rates in 0.1 M $[NBu_4]PF_6$ in MeCN.

Table S3. Electrochemical data from a 0.5 mM solution of complex **2** at different scan rates.

Scan rate (mV)	I_{pa}(µA)	I_{pc}(µA)	I_{pc}/I_{pa} [a]	E_{pa}(V)	E_{pc}(V)	$E_{1/2}$(V)
1000	15.01	10.70	0.71	0.368	0.233	0.301
750	12.47	9.30	0.74	0.366	0.233	0.299
500	10.47	7.59	0.72	0.356	0.233	0.294
200	6.78	4.95	0.73	0.351	0.236	0.293
100	5.01	3.25	0.65	0.348	0.241	0.294
50	3.97	2.64	0.66	0.346	0.243	0.294

[a] The I_{pc}/I_{pa} ratio of the redox process is fairly constant over a broad scan rate (Table 2). Together with the small potential difference between E_{pc} and E_{pa} (ΔE = ca. 120 mV), this indicates an E mechanism with a reversible redox process for complex **2** at +0.30 V (*vs* Fc^+/Fc).

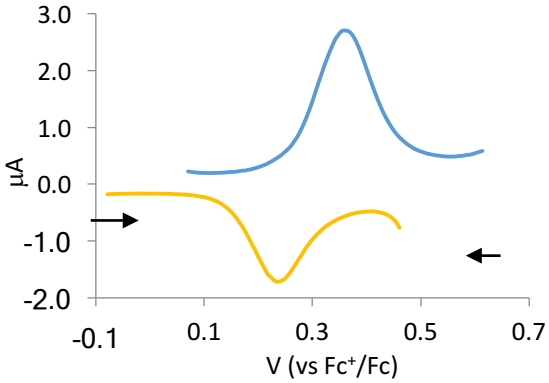

Figure S22. DPV oxidation (blue) and reduction (yellow) of 0.5 mM solutions of complex **2** in 0.1 M $[NBu_4]PF_6$ in MeCN (0.005 V step potential).

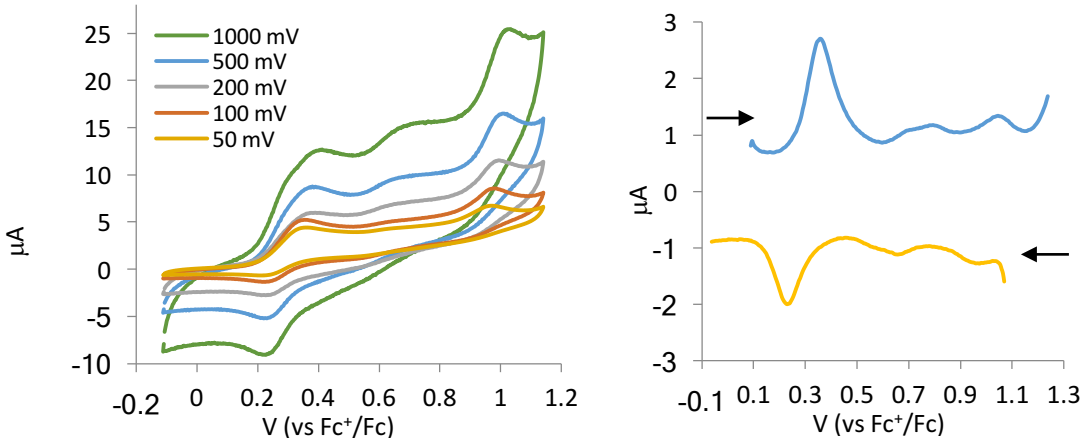

Figure S23. Left: Overlaid CV plots of 0.5 mM solutions of complex **2** at different scan rates in 0.1 M $[NBu_4]PF_6$ in MeCN in a larger potential window (–0.1 V to +1.14 V *vs* Fc/Fc^+) reveal further redox processes, although considerably less intense than the redox event at +0.30 V. Right: DPV oxidation (blue) and reduction (yellow) of complex **2** (0.005 V step change).

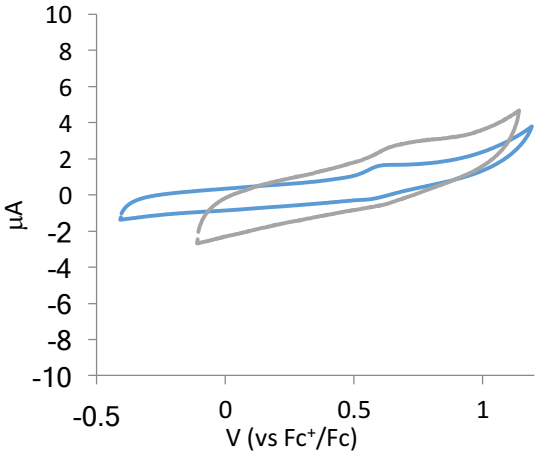

Figure S24. Overlaid CV plots of 0.5 mM solutions of the ligand precursor **1b** (grey), and blank solution (blue) in 0.1 M $[NBu_4]PF_6$ in MeCN (scan rate 500 mV s^{-1}) show that this compound is electrochemically inert in the–0.1 to +1.14 V potential range (*vs* Fc/Fc^+).

*Complex **3***

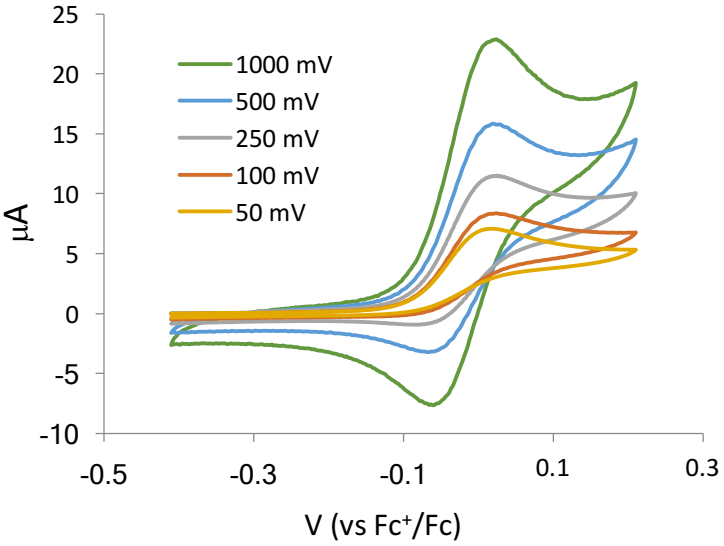

Figure S25. Overlaid CV plots of 0.5 mM solutions of complex **3** at different scan rates in 0.1 M $[NBu_4]PF_6$ in MeCN providing $E_{1/2}$ = –0.02 V *vs* Fc^+/Fc.

Table S4. Electrochemical data from a 0.5 mM solution of complex **3** at different scan rates.

Scan rate (mV s^{-1})	I_{pa}(μA)	I_{pc}(μA)	I_{pc}/I_{pa} [a]	E_{pa}(V)	E_{pc}(V)	$E_{1/2}$(V)
1000	22	16.2	0.73	0.022	–0.063	–0.021
500	15.3	9.7	0.63	0.019	–0.060	–0.021
250	11.15	6.09	0.54	0.017	–0.064	–0.023
100	7.99	3.64	0.45	–	–	–
50	6.77	3.64	0.54	–	–	–

[a] The gradual decrease of the I_{pc}/I_{pa} ratio suggests an EC mechanism. However, analysis of the current ratio (I_{pc}/I_{pa}) *vs* time does not correlate with a first or second order rate law, which may indicate that the electron transfer is not a fully reversible process, *i.e.* both E and C are not reversible.

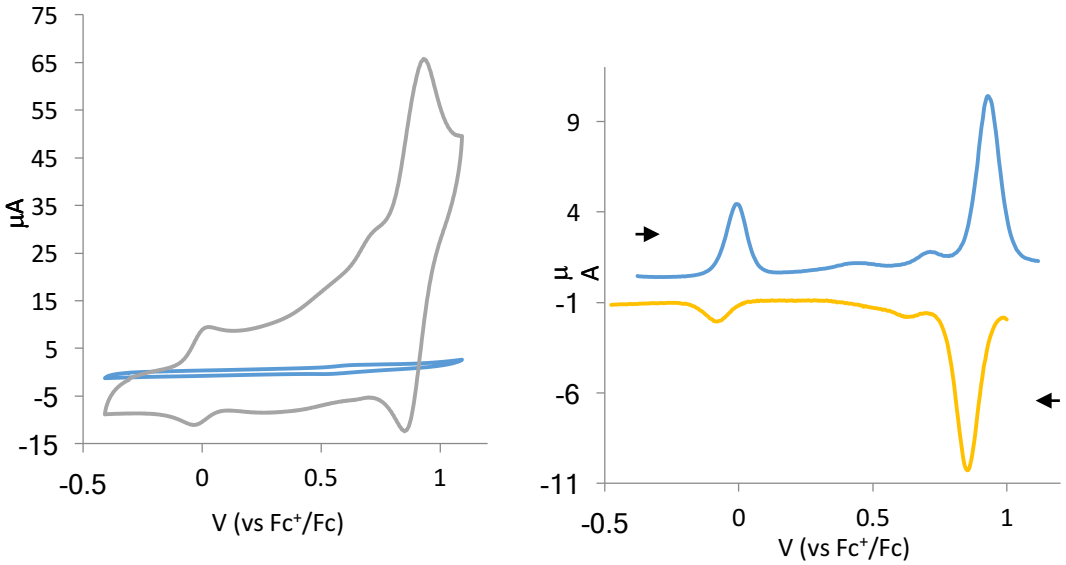

Figure S26. Measurement of complex **3** over a larger potential window (–0.5 to +1.12 V *vs* Fc^+/Fc). Left: Overlaid CV plots of 0.5 mM solutions of complex **3** and $[Ru(bpy)_3](PF_6)_2$ as internal standard (grey), and

blank solution (blue) in 0.1 M $[NBu_4]PF_6$ in MeCN, scan rate 500 mV s^{-1}. Right: DPV oxidation (blue) and reduction (yellow) with step potential = 0.005 V.

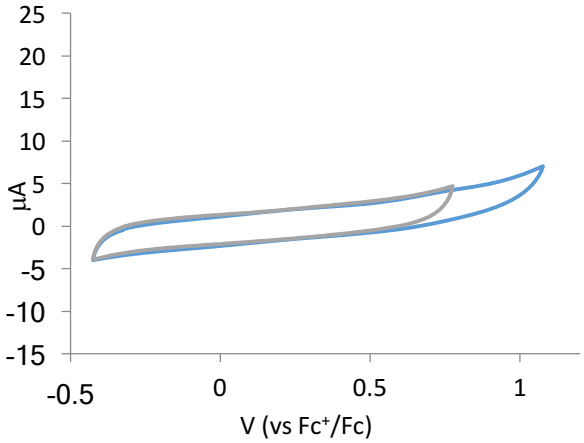

Figure S27. CV measurements of the ligand precursor **1a** (grey; blank solution blue) does not show any redox activity (2 mM di(triazolium) salt in 0.1 M $[NBu_4]PF_6$ in MeCN, scan rate 500 mV s^{-1}.

*Complex **4***

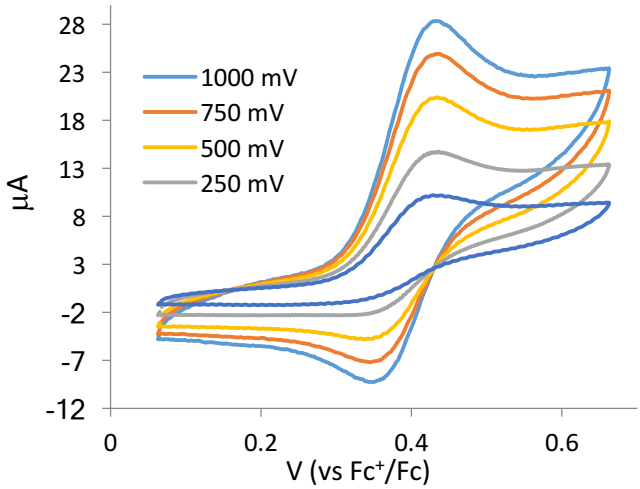

Figure S28. Overlaid CV plots of 0.5 mM solutions of complex **4** at different scan rates in 0.1 M $[NBu_4]PF_6$ in MeCN.

Table S5. Electrochemical data from a 0.5 mM solution of complex **4** at different scan rates.

Scan rate (mV s^{-1})	I_{pa}(µA)	I_{pc}(µA)	I_{pc}/I_{pa} [a]	E_{pa}(V)	E_{pc}(V)	$E_{1/2}$(V)
1000	26.46	19.78	0.748	0.431	0.348	0.389
750	23.23	15.8	0.680	0.431	0.346	0.388
500	19.26	11.55	0.600	0.434	0.339	0.386
250	13.82	5.94	0.435	0.428	0.350	0.389
100	9.51	–	–	0.426	–	–

[a] Analysis of the I_{pc}/I_{pa} ratio relative to the scan rate is in agreement with a first order chemical reaction of the oxidized species (linear correlation factor R > 0.99), thus suggesting an EC mechanism.

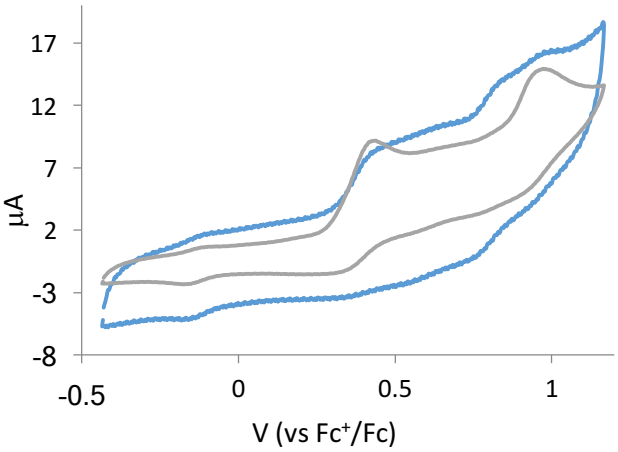

Figure S29. Overlaid CV plots of a fresh solutions of complex **4** (grey) and after standing for 40 min (blue; 0.5 mM complex, 0.1 M $[NBu_4]PF_6$ in MeCN, 100 mV s^{-1} scan rate) indicate that complex **4** decomposes over time. Also note that in a larger potential window three oxidation processes are observed at around –0.1 V, 0.4 V, and 0.9 V.

*Complex **5***

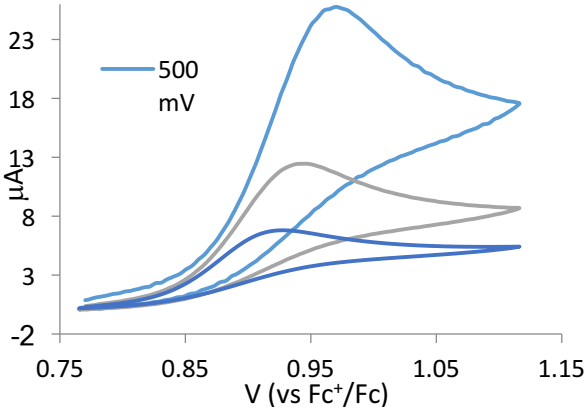

Figure S30. Overlaid CV plots of 0.5 mM solutions of complex **5** in 0.1 M $[NBu_4]PF_6$ in MeCN indicates an irreversible oxidation which depends on the scan rate with E_{pa} = +0.967 V (500 mV s^{-1}), +0.938 V (100 mV s^{-1}), and +0.921 V (25 mV s^{-1}), respectively (ferrocene as internal reference).

5. In operando IR analysis of alcohol oxidation

Time-resolved online MCT FT-IR spectra were recorded on a ReactIR 15 Instrument (Mettler Toledo) equipped with a diamond probe (DiComp, optical range of 3000–650 cm^{-1}). For online monitoring, the diamond probe was introduced into a glass tube (100 mm height, 12 mm diameter) containing the reaction mixture and spectra were recorded at specific times. Complex **3**, 1-phenylethanol, TBHP, mesitylene and acetophenone were recorded separately in MeCN at 40 ºC to simulate catalytic reaction conditions (Fig. S31–S35).

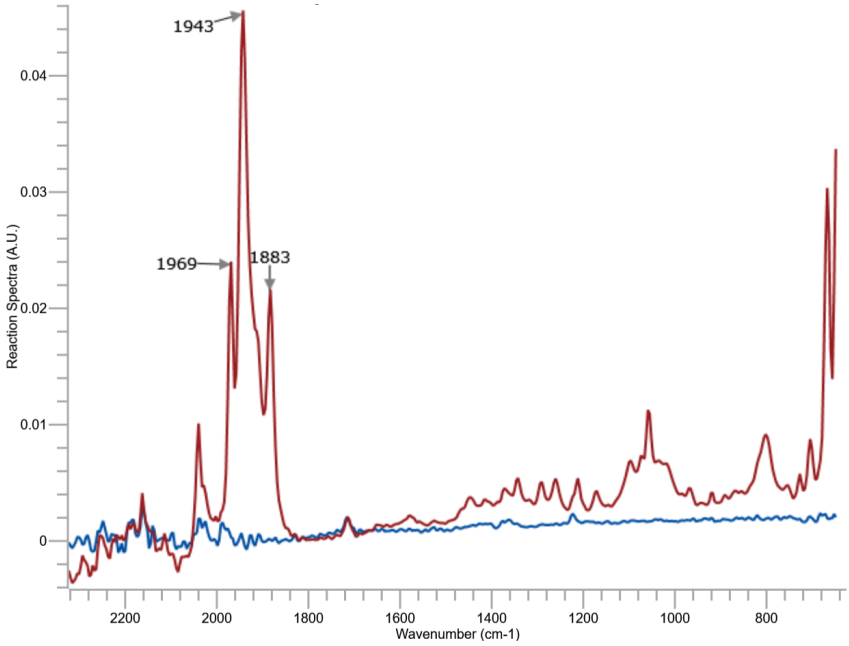

Figure S31. IR spectra of complex **3** in MeCN at 40 ºC (red) and pure solvent (blue).

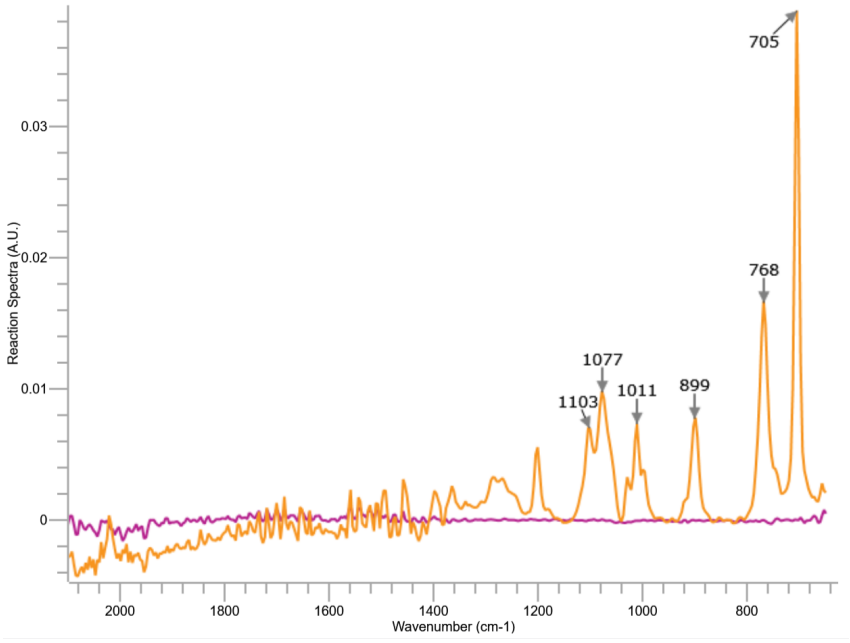

Figure S32. IR spectra of 1-phenylethanol in MeCN at 40 ºC (orange) and pure solvent (purple).

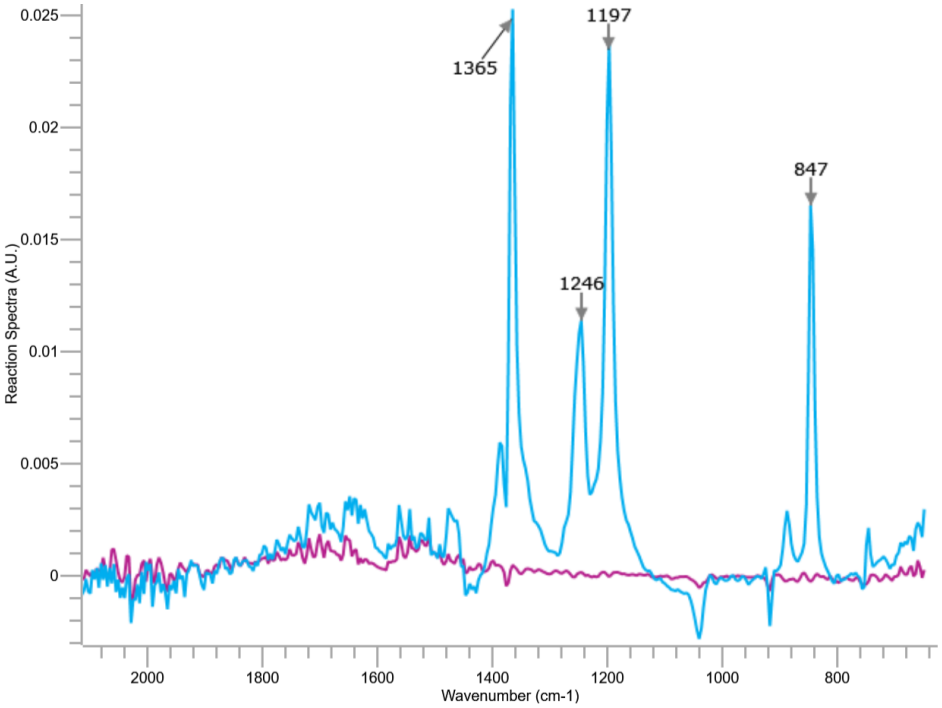

Figure S33. IR spectra of TBHP in MeCN at 40 ºC (blue) and pure solvent (purple).

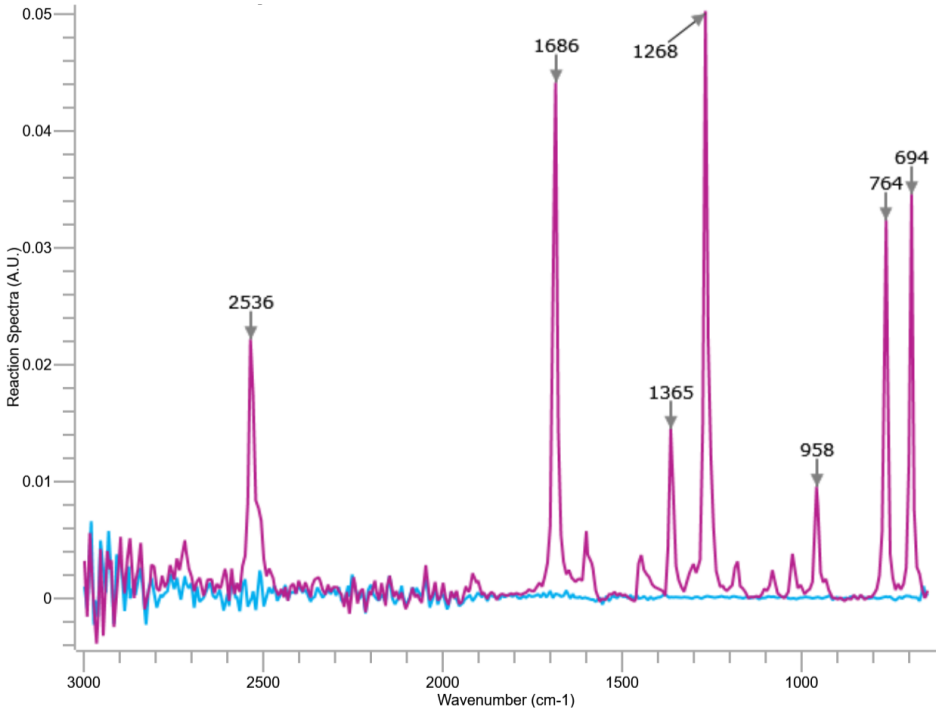

Figure S34. IR spectra of acetophenone in MeCN at 40 ºC (purple) and pure solvent (blue).

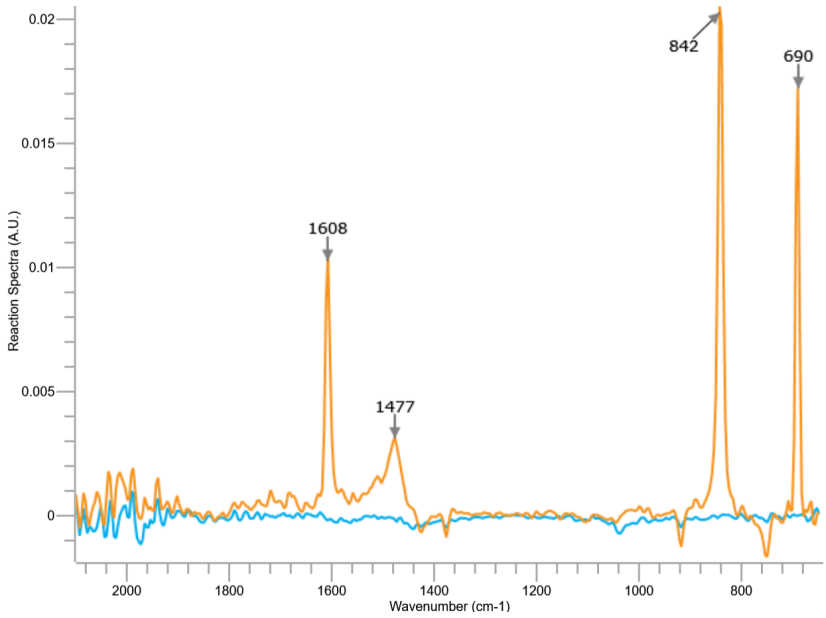

Figure S35. IR spectra of mesitylene in MeCN at 40 ºC (orange) and pure solvent (blue).

IR measurements under catalytic conditions

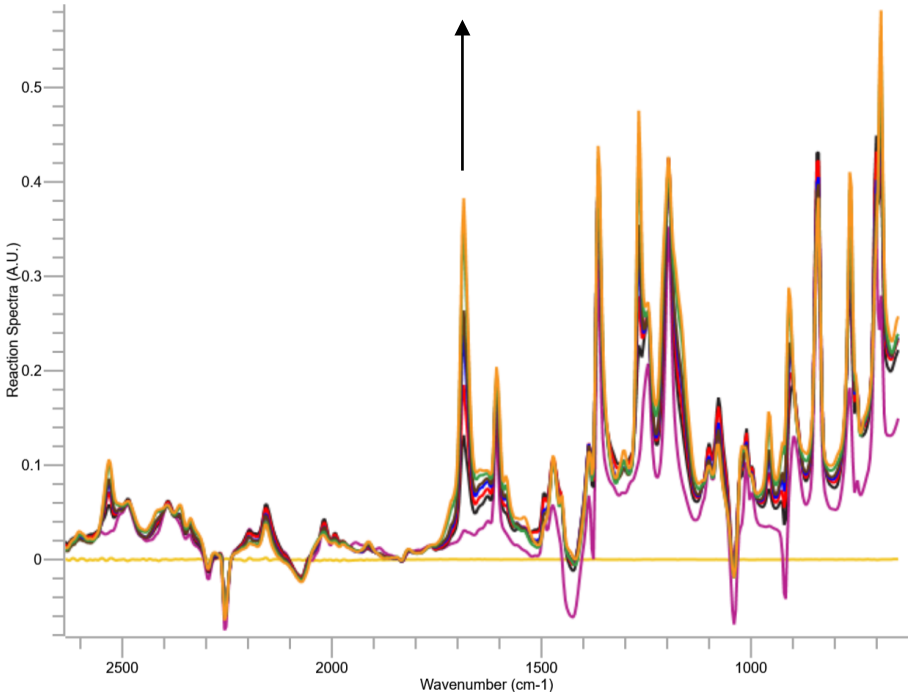

Figure S36. Superimposed IR spectra of the catalytic reaction using complex **3** at 40 ºC. IR spectra recorded at time 0 (purple), 30 min (black), 1 h (red), 2 h (blue), 3 h (brown), 16 h (green) and 24 h (orange). The IR band at 1686 cm^{-1} corresponds to acetophenone as the product of alcohol oxidation is detected already after 30 min and keeps increasing over the course of the reaction.

Conditions: Complex **3** (12 mg, 0.02 mmol), 1-phenylethanol (260 µL, 2.16 mmol), TBHP (650 µL, 3.24 mmol) and mesitylene (300 µL, 2.16 mmol) in MeCN (1 mL) were mixed. Mesitylene was added as internal standard. The reaction mixture was heated at 40 ºC and monitored by time-resolved online MCT FT-IR spectroscopy.

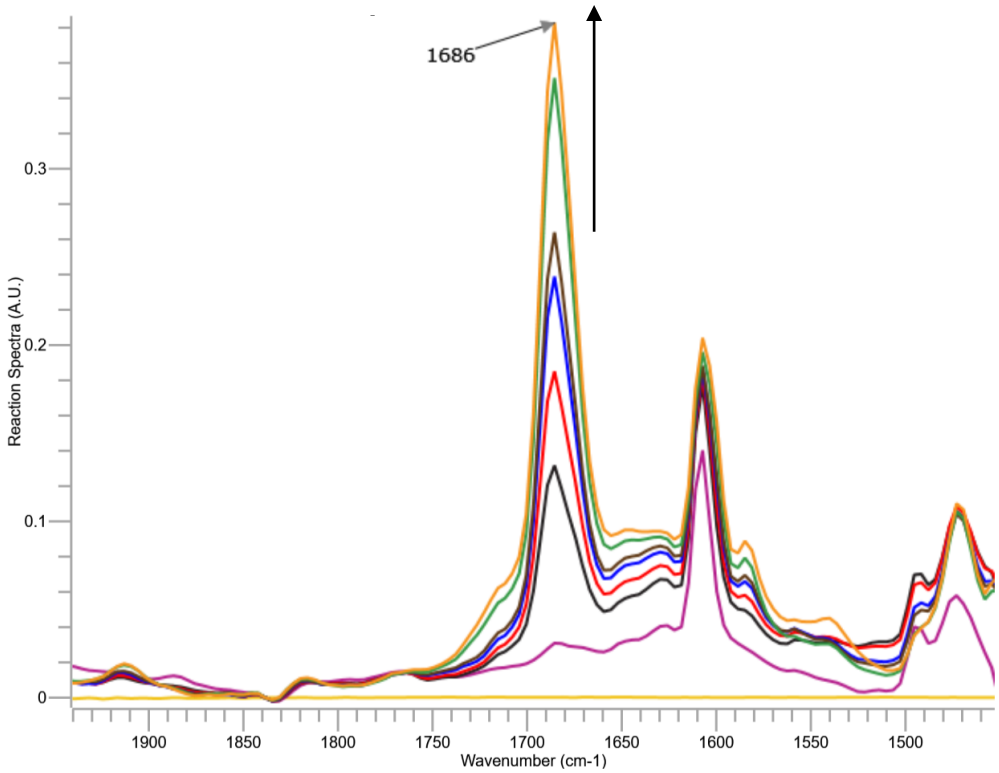

Figure S37. Expansion of the superimposed IR spectra in the 1450–1950 cm^{-1} range with IR spectra recorded at time 0 (purple), 30 min (black), 1 h (red), 2 h (blue), 3 h (brown), 16 h (green) and 24 h (orange). The starting material disappeared immediately (bands at 1943 and 1883 cm^{-1}) However, in the 1620–1660 cm^{-1} range, weak ill-defined bands evolve that were tentatively assigned to the active species (*cf* Fig. S39 below).

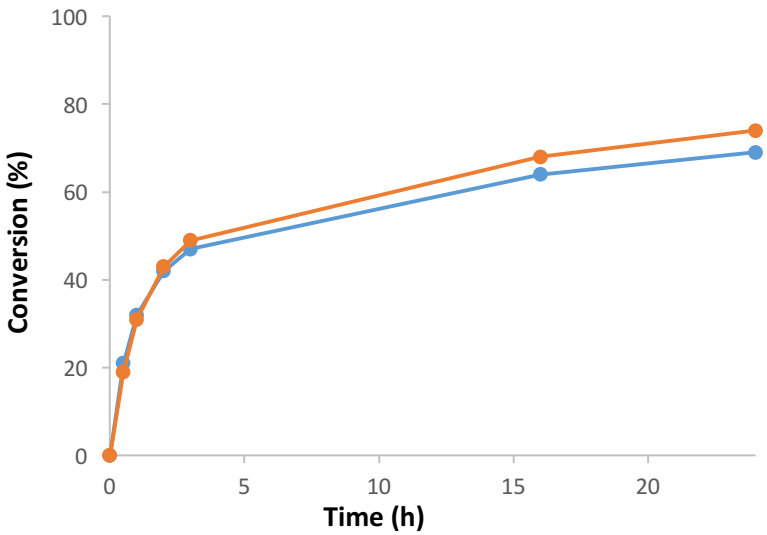

Figure S38. Catalytic profile for the oxidation of 1-phenylethanol using complex **3** under conditions as described in Fig. S36. Conversions were determined by ^{1}H NMR integration using mesitylene as internal standard (orange line) and time-resolved online MCT FT-IR spectroscopy. The height of the IR band at 1686 cm^{-1} (blue) shows an excellent correlation with conversions determined by ^{1}H NMR spectroscopy (Table S6).

Table S6. Conversions determined by IR and NMR spectroscopy for 1-phenylethanol oxidation catalyzed by complex **3**.

time (h)	conv. IR (%)	conv. NMR (%)
0	0	0
0.5	21	19
1	32	31
2	42	43
3	47	49
16	64	68
24	69	74

IR measurements under stoichiometric conditions

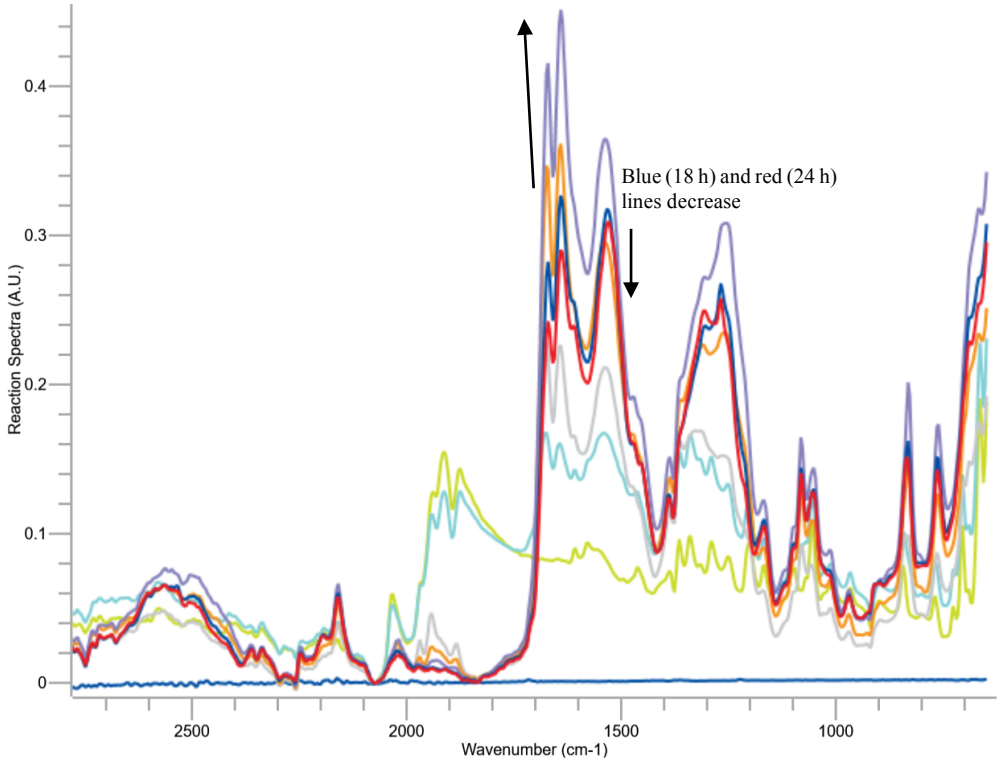

Figure S39. Superimposed IR spectra of the stoichiometric reaction using complex **3** at 40 ºC. IR spectra recorded at time 0 (green), 20 min (turquoise), 40 min (grey), 80 min (orange), 4 h (purple), 18 h (blue) and 24 h (red line). Conditions: Complex **3** (12 mg, 0.02 mmol), 1-phenylethanol (11 µL, 0.08 mmol), TBHP (17 µL, 0.08 mmol) and mesitylene (12 µL, 0.08 mmol) in MeCN (1 mL) were mixed. Mesitylene was added as internal standard.

The three IR bands for complex **3** at 1969, 1943 and 1883 cm^{-1} in MeCN rapidly deplete under stoichiometric conditions (1:4:4; complex:alcohol:TBHP) and eventually fully disappear. At the same time, three new IR bands appear at 1671, 1640 and 1534 cm^{-1} presumably from the active species that are shifted ca. 300 cm^{-1} for the first two bands and 350 cm^{-1} for the last band of the starting complex **3**. The new three IR bands steadily increase in intensity for the first 2 h. Then the intensity remains constant for approximately 3 h and starts to decrease after this time.

6. Crystallographic details

Crystals of **3** were grown by slow diffusion of Et_2O into a solution of the complex in CH_2Cl_2. A suitable crystal was mounted in air at ambient conditions. All measurements were made on an Oxford Diffraction SuperNova area-detector diffractometer[S20] using mirror optics monochromated Mo Kα radiation (λ = 0.71073 Å) and Al filtered.[S21] The unit cell constants and an orientation matrix for data collection were obtained from a least-squares refinement of the setting angles of reflections in the range 2.4° < θ < 27.7°. A total of 657 frames were collected using ω scans, with 5+5 seconds exposure time, a rotation angle of 1.0° per frame, a crystal-detector distance of 65.0 mm, at T = 123(2) K. Data reduction was performed using the CrysAlisPro program.[S20] The intensities were corrected for Lorentz and polarization effects, and a numerical absorption correction based on gaussian integration over a multifaceted crystal model was applied.
The structure was solved by direct methods using SHELXT[S22], which revealed the positions of all non-hydrogen atoms of the title compound. The non-hydrogen atoms were refined anisotropically. All H-atoms were placed in geometrically calculated positions and refined using a riding model where each H-atom was assigned a fixed isotropic displacement parameter with a value equal to 1.2Ueq of its parent atom (1.5Ueq for methyl groups). Refinement of the structure was carried out on F^2 using full-matrix least-squares procedures, which minimized the function $\Sigma w(F_o^2 - F_c^2)^2$. The weighting scheme was based on counting statistics and included a factor to downweight the intense reflections. All calculations were performed using the SHELXL-2014/74 program. Further crystallographic details are compiled in Table S5. Crystallographic data for this structure have been deposited with the Cambridge Crystallographic Data Centre (CCDC) as supplementary publication number 1895142. Selected bond lengths and angles are compiled in Table S7.

Table S7. Crystal data and structure refinement for **3**.

CCDC No.	1895142	
Empirical formula	$C_{18}H_{16}Mn_2N_6O_8$	
Formula weight	554.25	
Temperature	123(2) K	
Wavelength	0.71073 Å	
Crystal system	Monoclinic	
Space group	C 2/c	
Unit cell dimensions	a = 14.6208(2)Å	α = 90°
	b = 10.59240(10)Å	β = 108.231(2)°
	c = 15.2131(2)Å	γ = 90°
Volume	2237.78(5) $Å^3$	
Z	4	
Density (calculated)	1.645 Mg m^{-3}	
Absorption coefficient	1.186 mm^{-1}	
F(000)	1120	
Crystal size	0.353 x 0.154 x 0.106 mm^3	

Theta range for data collection	2.418 to 28.169°
Index ranges	−19 ≤ h ≤ 19, −14 ≤ k ≤ 13, −20 ≤ l ≤ 19
Reflections collected	10803
Independent reflections	2542[R(int) =0.0242]
Completeness to theta =37.399°	100%
Absorption correction	Gaussian
Max. and min. transmission	1 and 0.697
Refinement method	Full-matrix least-squares on F^2
Data / restraints / parameters	2542/ 0/ 156
Goodness-of-fit on F^2	1.077
Final R indices [I>2sigma(I)]	R1 = 0.0249, wR2 = 0.0619
R indices (all data)	R1 = 0.029, wR2 = 0.0648
Largest diff. peak and hole	1.372 and -0.276 e $Å^{-3}$

Table S6. Representative bond lengths [Å] and angles [°] for complex **3**.

Mn1-Mn1a	2.9389 (4)
Mn1-C6	1.8072(17)
Mn1-C7	1.8361(16)
Mn1-C8	1.7946(16)
Mn1-C9	1.8377(16)
Mn1-C1	2.0440(15)
C6-Mn1-C1	172.11(6)
C7-Mn1-C1	87.65(6)
C9-Mn1-C1	87.82(6)
C8-Mn1- Mn1a	173.93(5)
C6-Mn1- Mn1a	83.98(5)
C17- Mn1- Mn1a	82.40(5)
C9- Mn1- Mn1a	85.62(5)
C1- Mn1- Mn1a	88.12(4)

7. References

S1 G. Guisado-Barrios, J. Bouffard, B. Donnadieu and G.Bertrand, *Organometallics,* 2011, **36**, 6017–6021.

S2 A. Vivancos and M. Albrecht, *Organometallics*, 2017, **36**, 1580–1590.

S3 Y. Liu, K. S. Kjaer, L. A. Fredin, P. Chábera, T. Harlang, S. E. Canton, S. Lidin, J. Zhang, R. Lomoth, K.-E. Bergquist, P. Persson, K. Wärnmark and V. Sundström, *Chem. Eur. J.,* 2015, **21**, 3628–3639.

S4 F. Franco, M. Pinto, B. Royo and J. Lloret-Fillol, *Angew. Chem. Int. Ed*., 2018, **57**, 4603–4606.

S5 V. Vermaak, D. A. Young and A. J. Swarts, *Dalton Trans*., 2018, **47**, 16534–16542.

S6 G. Chen, L. Chen, L. Ma, H.-K. Kwong and Lau, *Chem. Commun*., 2016, **52**, 9271–9274.

S7 W. Dai, Y. Lv, L. Wang, S. Shang, B. Chen, G. Li and S. Gao, *Chem. Commun*., 2015, **51**, 11268–11271.

S8 K. Lagerblom, E. Lagerspets, J. Keskiväli, C. Cook, F. Ekholm, A. Parviainen and T. Repo, *ChemCatChem,* 2017, **9**, 3880–3887.

S9 K. Lagerblom, J. Keskiväli, A. Parviainen, J. Mannisto and T. Repo, *ChemCatChem*, 2018, **10**, 2908–2914.

S10 Z. Zhang, L. Khrouz, G. Yin and B. Andrioletti, *Eur. J. Org. Chem.,* 2019, 323–327.

S11 J.-D. Lou and Z.-N. Xu, *Tetrahedron Lett*., 2002, **43**, 6149–6150.

S12 A. Rezaeifard, M. Jafarpour, M. A. Nasseri and R. Haddad, *Helv. Chim. Acta*, 2010, **93**, 711–717.

S13 Murugavel, EurJIC 2018, 795

S14 I. Kani and S. Bolat, *Appl. Organometal. Chem*,, 2016, **30**, 713–721.
S15 M. M. Najafpour, M. Amini, M. Bagherzadeh, D. M. Boghaei and V. McKee, *Transition Met. Chem.,* 2010, **35**, 297–303.
S16 M. M. Najafpour, F. Ebrahimi, M. Amini, M. Rahimi, A. El-Sawy and S. L. Suib, *Dalton Trans.,* 2015, **44**, 15121–15125.
S17 D. Shen, C. Miao, D. Xu, C. Xia and W. Sun, *Org. Lett.*, 2015, **17**, 54–57.
S18 C. Miao, X.-X. Li, Y.-M. Lee, C. Xia, Y. Wang, W. Nam and W. Sun, *Chem. Sci.*, 2017, **8**, 7476–7482.
S19 M. T. Räisänen, A. Al-Hunaiti, E. Atousuo, M. Kemell, M. Leskelä and T. Repo, *Catal. Sci. Technol.*, 2014, **4**, 2564–2573.
S20 Oxford Diffraction (2010). CrysAlisPro (Version 1.171.38.41). Oxford Diffraction Ltd., Yarnton, Oxfordshire, UK.
S21 P. Macchi, H. B. Bürgi, A. S. Chimpri, J. Hauser and Z. Gal, *J. Appl. Cryst,*, 2011, **44**, 763–771.
S22 G. M. Sheldrick, *Acta Cryst.,* 2015, **A71**, 3–8.